Composite Structures 394 (2026) 120672

Contents lists available at ScienceDirect

Composite Structures

journal homepage: www.elsevier.com/locate/compstruct

Accelerating the prediction of strain-rate effect for carbon/epoxy composites using constitutive Artificial Neural Networks (CANNs)

Sanghyun Yoo [a,b,*], Ijaz Aslamsha [c], Dipankul Bhattacharya [d], Julia Kowalski [d], Nathalie Toso [a], Heinz Voggenreiter [a]

[a] *Institute of Structures and Design, German Aerospace Center (DLR), Stuttgart, Germany*
[b] *Innovation Center for Small Aircraft Technologies (INK), German Aerospace Center (DLR), Würselen, Germany*
[c] *Institute of Software Methods for Product Virtualization, German Aerospace Center (DLR), Dresden, Germany*
[d] *Chair of Methods for Model-based Development in Computational Engineering, RWTH Aachen University, Aachen, Germany*

ARTICLE INFO

Keywords:
Constitutive Artificial Neural Networks
Machine learning
Carbon-epoxy
Strain rate effect
Strength

ABSTRACT

The design of composite structures for impact and crash scenarios critically relies on understanding strain-rate effect, where mechanical properties significantly vary with the local loading rates of the material. Characterising the dynamic material responses of these materials for crashworthy design is traditionally resource-intensive. While standard data-driven machine learning (ML) models offer a convenient way to learn the underlying complex characteristics from experiments, they often lack physical consistency. Additionally, they are resource-intensive, requiring large volumes of experimental data. Circumventing these two issues, we propose a novel approach utilising Constitutive Artificial Neural Networks (CANNs) to characterise the strain-rate dependent behaviour of carbon/epoxy composites. Unlike existing black-box algorithms, this approach directly embeds constitutive equations into the neural network architecture. The model is tested for IM7/8552 under uniaxial compression at strain rates up to 200 s^{-1}. The model predictions demonstrate good agreement with experimental data (nRMSE = 7.3%), effectively capturing complex rate-dependent characteristics. Apart from demonstrating accurate interpolation, the model also shows robust extrapolation to out-of-distribution (OOD) strain rates. By combining the flexibility of ML with the reliability of physical laws, this approach significantly reduces the experimental burden, offering a powerful method to accelerate the design of safe and high-performance composite structures.

1. Introduction

The building block approach, also known as the test pyramid, has long been fundamental in the certification process of materials used in safety–critical aerospace applications. While this approach is essential for ensuring safety, it requires extensive testing to validate the safety and reliability. Validating material properties is inherently resource-intensive, especially at the coupon level and requires high costs and time-consuming experiments. Thus, this process imposes substantial time and cost burdens when a new material is introduced [1–3]. Additionally, the subsequent development of composite structures relies heavily on Finite Element (FE) simulations, which often demands high computational costs to achieve high-fidelity results in high-dimensional parameter spaces [4]. Given these challenges, there is an increasing demand for more effective methodologies. In this context, integrating Machine Learning (ML) can accelerate understanding of complex material behaviours and reduce the burden of data generation.

It is a well-known fact that polymer matrix composites are strain-rate sensitive [5–7]. Characterising strain-rate effects requires specialised dynamic testing set-ups such as Split Hopkinson Pressure Bars (SHPB) [5,6] or a high-speed servo-hydraulic machine [8] that are significantly more time-intensive than quasi-static tests. Consequently, a comprehensive understanding of structural integrity under high loading rates remains difficult to achieve due to the scarcity of dynamic material data. This pose challenge given that strain-rate sensitivity is crucial for the accurate design of composite structures subjected to impact and crash scenarios.

ML models have gained popularity in the prediction of material properties and material design parameters [9–18]. To recognise this potential, the aerospace industry is showing increasing interest to

* Corresponding author at: Institute of Structures and Design, German Aerospace Center (DLR), Stuttgart, Germany.
E-mail address: Sanghyun.Yoo@dlr.de (S. Yoo).

https://doi.org/10.1016/j.compstruct.2026.120672
Received 11 May 2026; Received in revised form 23 June 2026; Accepted 17 July 2026
Available online 18 July 2026

accelerate the development process of composite aero-structure by integrating ML models. This new paradigm seeks to invert the traditional reliance on physical tests by using ML models to explore the design space and predict structural performance, ultimately shortening development cycles [1]. For example, Shah et al. [17] predicted the modulus of elasticity of carbon-fibre reinforced polymers (CFRPs) using the Bimodal Recurrent Neural Network (RNN) model trained with over 6,500 experimental data obtained from the National Center for Advanced Materials Performance (NCAMP). They designed the Bimodal RNN model to handle the fibre orientation with long short-term memory (LSTM) branch while other categorical variables like curing cycles are handled by multi-layer perception (MLP) branch. It was found that the proposed model achieved a high R^2 score of 0.98, indicating strong predictive performance. However, purely data-driven models have inherent limitations. They are often requiring thousands of training data points, are data-hungry to estimate material parameters accurately, and struggle with out-of-distribution (OOD) predictions. Additionally, these approaches are purely empirical and function as black boxes, making it difficult to interpret results.

To overcome these bottlenecks, researchers are increasingly embedding physical laws into ML algorithms. The advantages of physics-integrated approaches such as Physics Informed Neural Networks (PINNs) [19–21] and Constitutive Artificial Neural Networks (CANNs) [22–24] require fewer data relative to traditional Artificial Neural Networks (ANNs) to train the model and possess an extrapolation capacity beyond the training range. In particular, the CANNs model is a novel machine learning architecture for a data-driven constitutive modelling that enables automatic model discovery for different materials. The CANNs bridge the gap between constitutive models and standard ANNs. The model integrates prior physical knowledge and the mathematical description of continuum mechanics is implemented in neural network design. Unlike ANNs, the CANNs model learns the strain energy density function ψ using invariants derived from continuum mechanics. Thus, the neural networks in the CANNs model process the information via invariants rather than directly mapping from strain to stress.

While the majority of research has focused on prediction of mechanical properties under quasi-static conditions, there is a distinct lack of studies addressing strain-rate dependency of fibre reinforced polymers (FRP) composites. The absence of reliable ML approaches to predict strain-rate effects of FRP composites creates open research questions that justify the need to develop physics-integrated data-driven modelling technique. This study addresses this gap by combining machine learning with constitutive laws to capture the rate-dependent behaviour of FRP composites. By leveraging the data extrapolability of CANNs, this approach aims at reducing the reliance on extensive dynamic testing at coupon level while still maintaining the necessary levels of reliability in material characterisation.

2. Experimental set-ups for data generation

2.1. Materials and specimen design

Test specimens were manufactured out of Hexply® IM7-8552, a unidirectional carbon-epoxy composite. Square 300 mm x 300 mm panels were first prepared in balanced cross-ply lay-ups of $[0°/90°]_{8s}$ to achieve a nominal thickness of 4 mm. The panels were cured under vacuum in an autoclave at 180 °C and 6 bar atmospheric pressure in accordance with the manufacturer's recommendations [25]. The use of cross-ply laminates is recommended to constrain the longitudinal plies under dynamic loading and help prevent premature failure [6].The post manufacturing quality of the panels was investigated with ultrasonic (US) scanning using an Olympus Omniscan MX2 device. Finally, the desired specimen geometries were machined out using a CNC high-pressure water jet cutting system (WARICUT HWE-P6040/1, H.G. RIDDER GmbH, Germany).

2.2. Experimental set-ups

Compression tests were performed at five nominal strain rates ranging from 1.67 $\times$ 10^{-3} s^{-1} to 200 s^{-1} (refer to Table 1). Uniaxial compression testing was performed using an internally designed fixture in which honeycomb is used to prevent sample instability [26]. The fixture was successfully used in a previous study of compression testing using carbon fibre-reinforced low-melt polyaryletherketone (CF/LM-PAEK) [8]. Five tests were conducted for each strain rate at both quasi-static and dynamic regimes using the same test fixture.

Fig. 1 (a) and (b) show the experimental set-up for the quasi-static and dynamic compression testing as well as the specimen geometry with dog-bone shape. The summary of the experimental settings like frame rates is reported in Table 1. The quasi-static compression tests were performed using a Zwick/Roell 1475 universal testing machine (UTM). The loading was applied under displacement control at a rate of 1 mm/min up to failure, equivalent to strain rate of 1.67 $\times$ 10^{-3} s^{-1}. A 3D Digital Image Correlation (DIC) stereo system (Q-400, LIMESS Messtechnik u. Software GmbH, Germany) was used to obtain full field deformation images. Acquired images were post-processed with INSTRA 4D software from Dantec Dynamics. Furthermore, for dynamic compression testing, an Instron® VHS 100/20 high-speed servo-hydraulic testing machine was used with a piezo-electric load cell with a capacity of $\pm$ 120 kN (Kistler-9317B, Kistler Instrumente GmbH, Germany). The force signals were amplified with a Kistler type 5011B charge amplifier. DIC images were captured using a high-speed camera (FASTCAM SA-Z, Photron®, Japan) with adjusted frame rates and resolutions to obtain sufficient images during the testing at different strain rates. These images were subsequently analysed using ZEISS INSPECT Correlate software from Carl Zeiss GOM Metrology GmbH to track the damage progression in the test specimens. In addition, the high-speed images were synchronised with the force signals through NI-DAQ (USB-6251 BNC, National Instruments™, USA).

It is worth mentioning that strain measurements from strain gauges were used to train the CANNs model while DIC measurements were used to verify the deformation and failure modes of the specimens. The DIC is not employed for input strain data since the CANNs model requires strain in both longitudinal and transverse directions. The use of strain gauges was necessary to measure in-plane strain in x and y directions as the DIC was performed in the through-the-thickness direction. Two types of strain gauges (FLAB −3–11-1 L and FLCA-3–11-1 L from Tokyo Sokki Kenkyujo Co., Ltd, Japan) were attached on both sides of the specimens. The output voltage was acquired using a strain gauge amplifier (SGA-2 MK2, Elsys AG, Switzerland), and strain was calculated from the output voltage with a full bridge configuration.

3. Modelling framework

The original CANNs model has been successfully demonstrated for hyperelastic constitutive models and the source code is publicly available under an MIT licence [22]. In this study, the original CANNs model is extended to predict strain-rate effects in FRP composites. The test material is assumed to exhibit orthotropic behaviour with two preferred directions as the through-the-thickness direction is redundant [27]. First, a constitutive orthotropy model is introduced into the network

Table 1
Summary of testing condition for dynamic compression testing including digital image correlation (DIC) settings.

Strain rates [s^{-1}]	Testing speed [mm/s]	Resolution [pixels]	Frame rates [fps]
QS1 (1.67 $\times$ 10^{-3})	0.0167	3000 $\times$ 992	2
QS2 (0.1)	1	1024 $\times$ 400	250
IR 1 (10)	100	1024 $\times$ 400	20 k
IR 2 (100)	1000	768 $\times$ 144	150 k
IR 3 (200)	2000	768 $\times$ 96	200 k

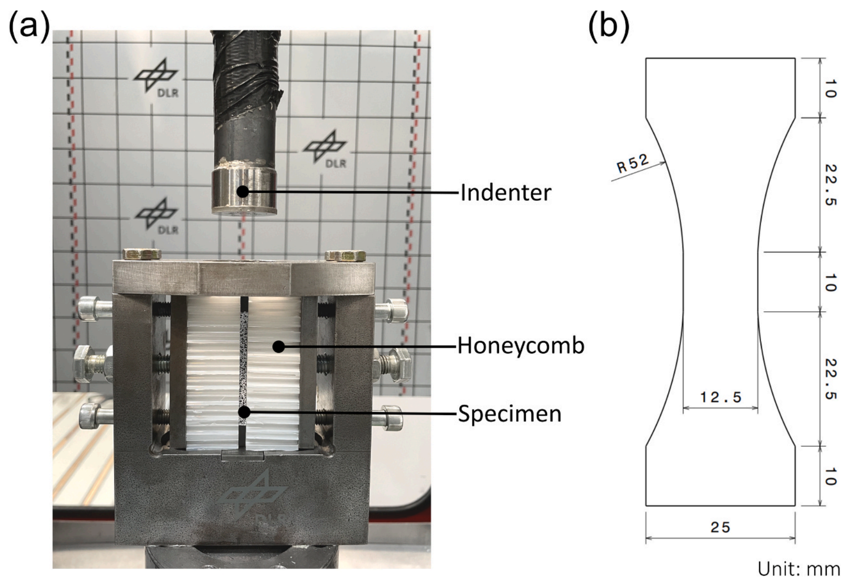

Fig. 1. (a) dynamic compression test set-up for end loading configuration and (b) specimen geometry for compression loading case.

architecture in Section 3.1. Hence, the constitutive equations for an orthotropic material as well as the strain-rate tensors are incorporated into the neural network design. Secondly, the implementation of Invariant-based Quadratic failure Criterion (IQC) is introduced in Section 3.2. Finally, the architecture of the CANNs model (invariants as input and strain energy density function as output) is presented in Section 3.3. The details on the computational settings for the implementation of the CANNs model are summarised in Table 2.

Fig. 2 shows the workflow for the CANNs model-based prediction. The input training dataset is first collected from the raw experimental stress–strain data. Next, the training data is processed using even-spaced sampling to standardise the varying vector lengths present in the raw data. After training, the strain vector is extrapolated by 35% using linear fitting to produce a uniform set of 200 data points, which allows the clear visualisation of the failure prediction point. The training dataset is split into an 80:20 ratio. It should be noted that the experimental data at a strain rate of 100 s^{-1} are excluded from the training dataset as they are used for validation. Finally, the CANNs model is trained using the processed data. For stress prediction, sub-ANN is trained on stress as a function of strain and strain rate. For failure prediction, the sub-ANN is trained on IQC as a function of strain-rate, strain and stress. After training and validation, the outputs are plotted on stress–strain curves across a wide range of strain rates.

Table 2
Summary of computational settings to run Constitutive Artificial Neural Networks (CANNs).

	Specifications
Computer	Dell Precision 7920 Tower
CPU	112 Intel(R) Xeon(R) Platinum 8280 CPU @ 2.70 GHz
GPU	NVIDIA RTX A6000
Main Python libraries	Tensorflow 2.15.0 and Keras 2.15.0
Activation functions	Linear for invariants, and Softplus for strain-rate tensor
Optimiser	keras.optimizers.Adam with learning rate of 0.05
Loss function	Mean Squared Error (MSE)
Number of trainable parameters	36 (weights and biases for invariants)
Computational time for training	≅ 5 min

3.1. Constitutive model for orthotropy

In the context of continuum mechanics of anisotropic materials, the structural tensors define the preferred material orientations. Consequently, the preferred directions of the material are incorporated through the structural tensors and orthotropic behaviours of carbon/epoxy composites in cross-ply laminate subjected to compression loading can be described through structural tensors, A_1 and A_2:

$$A_1 = a_1 \otimes a_1 \text{ and } A_2 = a_2 \otimes a_2 \tag{1}$$

The behaviour of an orthotropic FRP composites can be modelled using the strain energy density function. The strain energy density can be represented as a function of linear combination of invariants and can be modelled as individual sub-ANNs [23]. The invariants are composed of strain tensors and structural tensors. In addition, the strain energy density for an orthotropic material with two preferred directions can be given as the linear combination of the trace of the invariants and nine elasticity parameters $(\lambda, \mu, \alpha_1, \alpha_2, \mu_1, \mu_2, \beta_1,\ \beta_2, \text{and}\, \beta_3)$ to describe the orthotropic material behaviour [28,29].

Strain energy density function ψ is defined as:

$$\psi(E, A_1, A_2) = \frac{1}{2}\lambda(trE)^2 + \mu\left(tr\left(E^2\right)\right) + (\alpha_1 EA_1 + \alpha_2 EA_2)trE + 2\mu_1\left(E^2\right)A_1 + 2\mu_2\left(E^2\right)A_2 + \frac{1}{2}\beta_1(EA_1)^2 + \frac{1}{2}\beta_2(EA_2)^2 + \beta_3(EA_1)(EA_2) \tag{2}$$

The stress tensor can be derived by computing the first order derivative of the strain energy function with respect to the strain tensor, and it can be defined as:

$$\sigma = \frac{\partial\psi(E, A_1, A_2)}{\partial E} \tag{3}$$

where, $E = \begin{bmatrix} \varepsilon_{xx} & 0 & 0 \\ 0 & \varepsilon_{yy} & 0 \\ 0 & 0 & \varepsilon_{zz} \end{bmatrix}$, $A_1 = \begin{bmatrix} 1 & 0 & 0 \\ 0 & 0 & 0 \\ 0 & 0 & 0 \end{bmatrix}$, and $A_2 = \begin{bmatrix} 0 & 0 & 0 \\ 0 & 1 & 0 \\ 0 & 0 & 0 \end{bmatrix}$

3.2. Invariant-based Quadratic failure criterion (IQC)

The failure of FRP composites can be distinguished between two categories, Fibre Failure (FF) and matrix-dominated Inter-Fiber Failure (IFF) [27]. The fibre failure is defined as [30]:

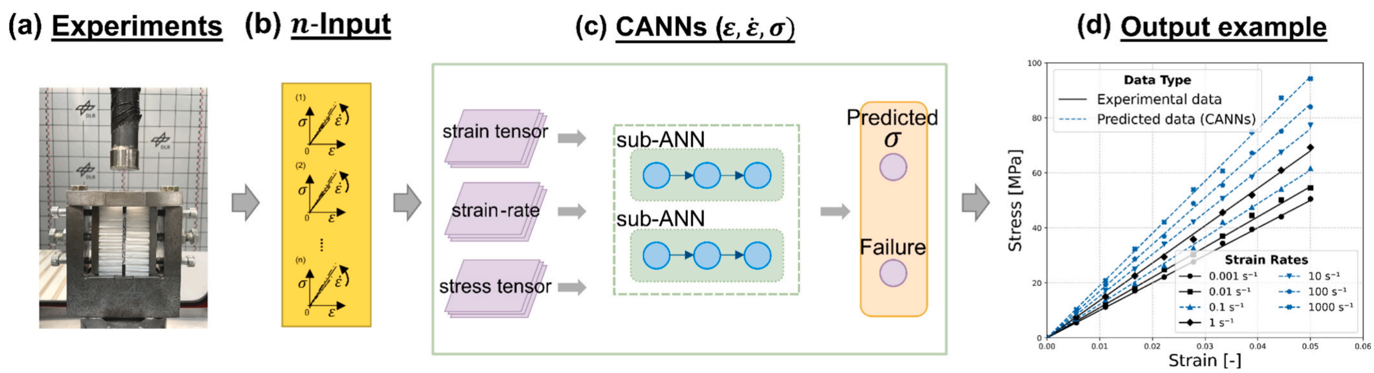

Fig. 2. Overview of data-driven modelling framework incorporating the Constitutive Artificial Neural Networks (CANNs) model: (a) input data generation by experimental compression testing; (b) multiple stress–strain data measured at different strain rates as input; (c) a CANNs model architecture; (d) an example of predicted stress–strain data from the CANNs model as output along with synthetic experimental results.

$$r_{fibre}(\sigma, \mathrm{A}) = \frac{a\sigma a}{X} - 1 \tag{4}$$

where the fibre failure criteria are fulfilled if r_{fibre} is equal or less than 0 and X is either the failure compressive X_c or tensile strength X_t of the fibre. The term $a\sigma a$ is the projection of the stress tensor onto the preferred direction a [27,30].

It should be noted that the fibre failure is excluded in this study since the force under which FF might occur is much higher than the threshold for IFF. The invariant-based Quadratic Failure Criterion (IQC) [27,30,31] is integrated into the design of CANNs architecture as it is based on an invariant, thereby enabling the direct integration and interpretable weight updates during training. For an orthotropic material, a decomposition of the stress tensor σ into plasticity including stress σ^p and reaction stress σ^r is assumed as:

$$\begin{aligned}\sigma^r &= (tr\sigma - a_1\sigma a_1 - a_1\sigma a_1)1 - (tr\sigma - 2a_1\sigma a_1 - a_2\sigma a_2)A_1 \\ &\quad - (tr\sigma - a_1\sigma a_1 - 2a_2\sigma a_2)A_2\end{aligned} \tag{5}$$

$$\sigma^p = \sigma - \sigma^r \tag{6}$$

With the stresses σ^p, the quadratic stress invariants are given as:

$$I_1 = tr(\sigma^p)^2 - a_1(\sigma^p)^2 a_1 - a_2(\sigma^p)^2 a_2 \tag{7}$$

$$I_2 = a_1(\sigma^p)^2 a_1 \tag{8}$$

$$I_3 = a_2(\sigma^p)^2 a_2 \tag{9}$$

Invariant I_4 controls the non-symmetric yielding known as Bauschinger effect by incorporating the hydrostatic pressure [25]:

$$I_4 = tr\sigma \tag{10}$$

Invariants I_5 and I_6 accounts for the effects of direction specific deviatoric stress σ^{dev} [29]:

$$I_5 = \frac{3}{2} a_1 (\sigma^{dev}) a_1 \tag{11}$$

$$I_6 = \frac{3}{2} a_2 (\sigma^{dev}) a_2 \tag{12}$$

Finally, the matrix failure f_m is determined when it is larger than 0. The extended orthotropic failure criterion based on stress invariants I_i built with σ^p, σ^r and σ^{dev} yields:

$$f_m = \alpha_1 I_1 + \alpha_2 I_2 + \alpha_3 I_3 + \alpha_5 I_5^2 + \alpha_6 I_6^2 + \alpha_7 I_5 I_6 + \alpha_4 I_4^3 + \alpha_8 I_4^2 I_5 + \alpha_9 I_4^2 I_6 - 1 \leq 0 \tag{13}$$

The formulation for estimating the parameters is given in Appendix A.

3.3. Constitutive Artificial Neural Networks (CANNs)

The strain obtained from the experiments is converted into strain tensors and those tensors are used to algebraically compute the components of the strain energy density, which are later converted to predicted stress tensors. Additionally, the strain-rate effect in FRP composites is introduced in the CANNs model by including a strain-rate tensor. Since logarithmic behaviour is expected based on literature [30,32], a strain-rate tensor is implemented with a base-10 logarithmic scaling that compresses the wide range of strain rates and an offset log scaling of 0.1 to prevent zero or negative values. The strain-rate tensor is defined as:

$$\dot{\varepsilon}_{scaled} = log_{10}(\dot{\varepsilon} + 0.1) \tag{14}$$

Fig. 3 illustrate the detailed CANNs architecture implemented for this study. The CANNs model comprise two blocks, namely the Psi computational block and the failure prediction block. While both blocks are trained on data extracted from the experiments described in Section 2, the inputs differ once the model is trained. The Psi computational block receives vectors of the strain tensor E and the strain-rate tensor $\dot{\mathrm{E}}$ across the entire stress–strain curve for each experiment. The neural network is trained to predict the corresponding stress values as its output using a supervised learning approach with a loss function that minimises the error between the predicted and experimental stress values. Once trained, the output of the Psi computational block is fed to the failure prediction block. Meanwhile, the failure prediction block is trained using experimental failure points, corresponding strains, and a given strain-rate. After both blocks are trained, they are sequentially combined. The output of the Psi computational block is the stress prediction. Then, the predicted stress–strain curves serve as input to the trained IQC failure model (i.e., the failure prediction block). The failure model subsequently predicts a stress–strain curve where the failure might occur.

Strain invariants in the 'Psi computational block' are passed into the Psi sub-ANNs that is responsible for learning the elasticity parameters in the strain energy density function. The outputs of the Psi sub-ANNs in Eq. (15) are combined with a linear activation function. Stress is then computed using automatic differentiation in TensorFlow, as defined in Eq. (16).

$$\text{Lamba layer 1}: \hat{I}_i = [w_{1,i} \bullet I_i] \cdot f(w_{2,i}, \dot{\varepsilon}) \tag{15}$$

$$\text{Lamba layer 2}: \psi = \sum_{i=1}^{n=9} \hat{I}_i; \sigma_{predicted} = \frac{\partial \psi}{\partial E} \tag{16}$$

The 'failure prediction block' takes as input a combined tensor

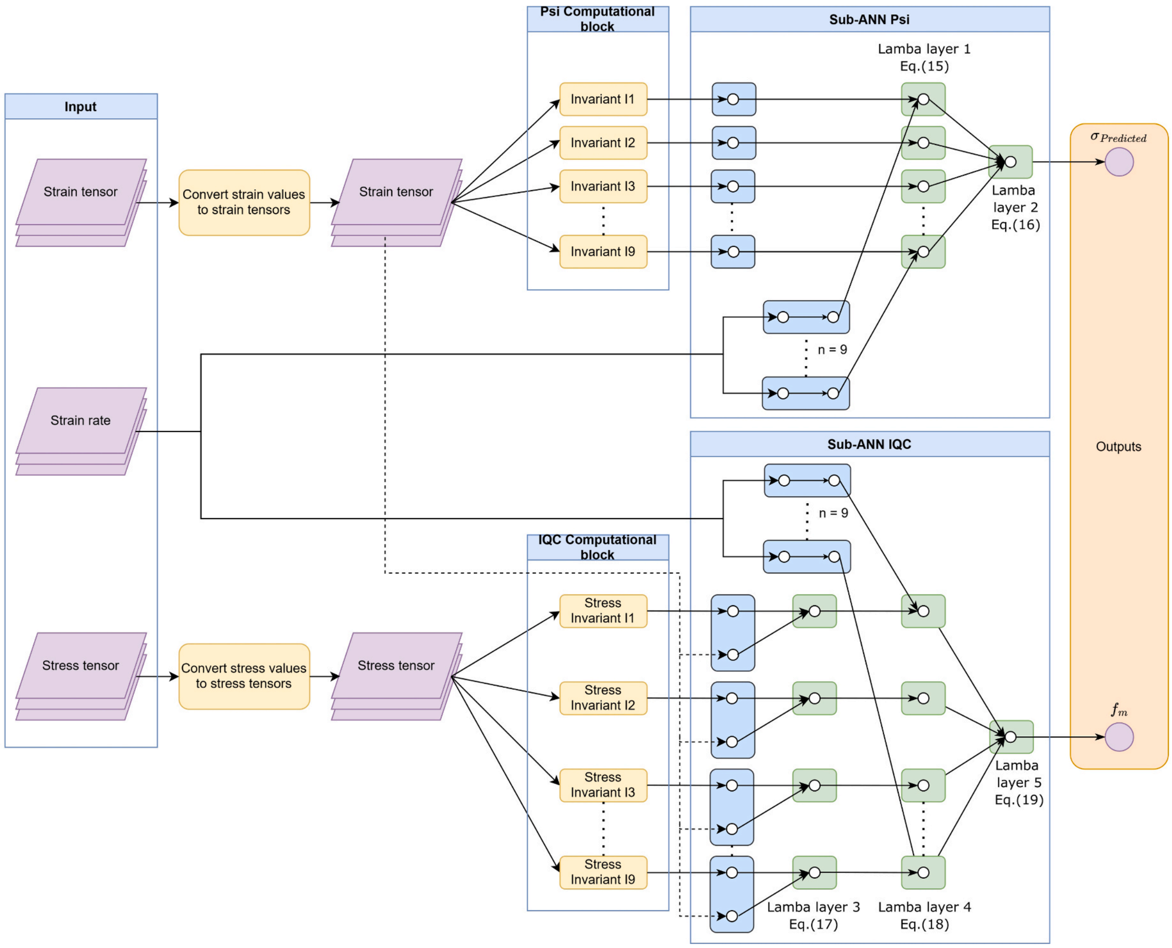

Fig. 3. Detailed flowchart for a CANNs network for prediction strain-rate dependent compression properties.

consisting of the compressive strength and failure strain, and the corresponding strain-rate for each test. The compressive strength from each experiment is used to compute σ_r and σ_p as defined in Eqs. (5) and (6), respectively. Stress tensors are used to compute the invariants described in Eqs. (7)-(12). These invariants are processed individually by their respective sub-ANNs to compute corresponding the material

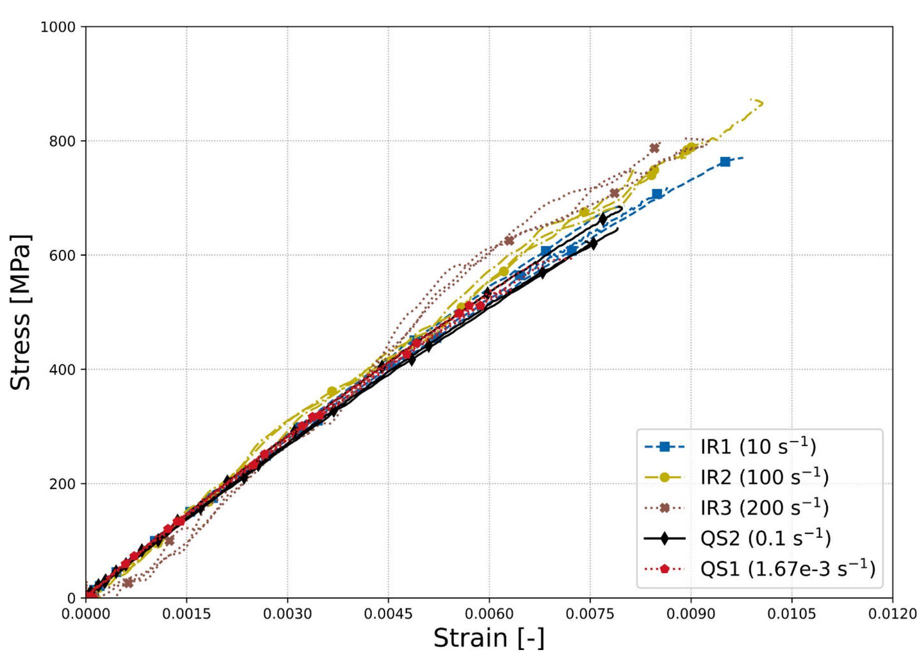

Fig. 4. Dynamic compression stress–strain data measured at strain-rates up to 200 s^{-1}.

parameters, which are subsequently combined through a lambda layer following Eq. (17). The network is trained to predict the inter-fibre failure f_m, optimising the model parameters via a loss function that minimises the difference between the predicted and experimental failure strength.

$$\text{Lamba layer } 3: I^{\sigma}_{i,combined} = \left[w_{1,i} \bullet I^{\sigma}_{i}\right] + \left[w_{1,i+1} \bullet \varepsilon\right] \tag{17}$$

$$\text{Lamba layer } 4: \widehat{I}^{\sigma}_{i,combined} = I^{\sigma}_{i,combined} \cdot f\left(w_{2,i}, \dot{\varepsilon}\right) \tag{18}$$

$$\text{Lamba layer } 5: f_m = \sum\nolimits_{i=1}^{n=9} \widehat{I}^{\sigma}_{i,combined} - 1 \tag{19}$$

4. Experimental data

Fig. 4 shows the compression stress–strain data measured from strain-rates ranging from quasi-static (1.67×10^{-3} s^{-1}) to intermediate strain rates (200 s^{-1}). The results reveal that there is a little strain-rate dependence on the compressive modulus, while the strength increases at increasing strain rate. This behaviour is analogous to observations reported in the literature [6,8,30,32], and the summary of experimental results is presented in Table 3. It should be noted that filters such as low-pass filters must be carefully applied, as they can distort the signal [33]. Thus, the raw stress–strain data is reported here without any post-processing although a slight oscillation is observed at strain rate of 200 s^{-1}.

5. Results

5.1. Normalised Root mean Squared Error (nRMSE)

The Root Mean Squared Error (RMSE) is normalised to quantify the variance across the different datasets used in this study and provides a dimensionless metric that enables an unbiased comparison. The normalised RMSE (nRMSE) by the mean is defined as:

$$\text{nRMSE} = \frac{\sqrt{\frac{1}{n}\sum_{i=1}^{n}\left(y_i - \widehat{y}_i\right)^2}}{\overline{y}} \tag{20}$$

where, n is the total number of data points, y_i is a data point in the experimental or literature data, $\widehat{y}_i$ is a data point in the CANNs-predicted data, and $\overline{y}$ is the mean of the experimental or literature data.

5.2. Predictions from the CANNs model

Fig. 5 shows different types of predictions made by the CANNs model to validate its prediction capability. The comparison between experimental and predicted data from the CANNs model at a strain rate of 100 s^{-1} is represented in Fig. 5 (a). This comparative study is to demonstrate the model's ability to accurately interpolate the compressive behaviour of IM7/8552 composites within the training domain. In this validation case, experimental data for the intermediates strain rate at 100 s^{-1} is explicitly excluded from the training dataset (denoted interpolation). This prediction is the one of the key capabilities of the CANNs model since it predicts the stress–strain response at the unseen strain-rate based on the patterns learned from other strain-rates (e.g., 0.1 s^{-1}, 10 s^{-1}, and 200 s^{-1}). Experimental data shows a mostly linear elastic region with non-linearity at close to the point of the failure. This nonlinearity appearing near the point of failure may indicate the onset of plastic deformation prior to rupture. Despite this nonlinearity, the CANNs predicted data captures the overall stress–strain behaviour of experimental data while the CANNs model makes predictions under the assumption of ideal linearity. This observation confirms that the physics-informed architecture has successfully generalised the strain-rate dependent constitutive laws.

Furthermore, Fig. 5 (b) presents the robust extrapolation capacity of the CANNs model, conforming its performance on prediction of OOD data. The compressive strength at strain-rates at 300 s^{-1} and 500 s^{-1} (denoted extrapolation) are predicted to examine the capacity of OOD prediction significantly outside the range of the experimental training dataset. This result follows the expected rate-dependent trend that the carbon/epoxy composites exhibit slightly increased stiffness and increasing failure strength compared to that of lower strain rates [5,6]. Unlike purely data-driven black-box models, which often behave erratically when making OOD predictions, the CANNs model maintains predictive capabilities with embedded constitutive models. This observation demonstrates that the model has successfully learned the underlying rate sensitivity of carbon/epoxy composites. This capability is critical to generate dynamic stress–strain dataset where strain-rates require for simulating crash and impact scenarios.

Fig. 6 (a) and (b) present the performance of CANNs model and determination of failure strength using the Invariant-based Quadratic failure Criterion (IQC), respectively. The selected dynamic stress–strain data of IM7/8552 and corresponding IQC analysis are provided as illustrative examples. In Fig. 6 (a), the orange diamond markers on the predicted stress–strain data from the CANNs model indicate the estimated failure points, which are mathematically derived from the IQC curves presented in Fig. 6 (b). The failure is triggered when the matrix failure f_m , exceeds the threshold of 0 indicated by the horizontal orange dashed line in accordance with to Eq. (13). Furthermore, Fig. 6 (c) and (d) compare the experimental compressive stress–strain behaviour of IM7/8552 at strain-rates ranging from quasi-static to intermediate strain-rates, with predictions from the CANNs model. These figures show that the CANNs predicted stress–strain data has learned and captured the overall stress–strain behaviours from experimental data at various strain-rates.

Given that neural networks are fundamentally stochastic, weight initialisation influences the convergence of the loss during model training. Consequently, neural networks typically start with randomly initialised weights, which directly affect the network's performance [34]. To address this variation, the predictions reported here are based on an ensemble of approximately 50 runs, ensuring the stability of the network's output. As a result, the resulting compressive moduli and failure strengths derived from this analysis are summarised in Table 4 and 5.

In addition, the CANNs model successfully captures the overall stress–strain relationships and underlying strain-rate effect. When compared to experimental results, the model prediction shows comparatively good agreement, predicting failure strength within a 6% difference. Although the difference in compressive modulus reaches approximately 18% at higher strain-rates, the model accurately captures the underlying strain-rate effect of carbon/epoxy composites given the complexities of dynamic testing. This discrepancy is likely due to the force oscillation during testing (refer to Section 4) and could be mitigated with further frequency analysis and experimental validation.

Table 3
Summary of quasi-static and dynamic compression properties of carbon/epoxy composites in nominal strain-rate range from 1.67×10^{-3} to 200 s^{-1}.

Strain rates [s^{-1}]	Compressive modulus [GPa]	Compressive strength [MPa]	Failure strain [-]
QS1 (1.67×10^{-3})	91.1 ± 0.8	582.0 ± 26.5	0.017 ± 0.001
QS2 (0.1)	89.0 ± 2.1	655.2 ± 26.0	0.018 ± 0.001
IR 1 (10)	90.2 ± 1.9	723.4 ± 42.1	0.018 ± 0.002
IR 2 (100)	108.1 ± 5.4	832.8 ± 48.9	0.020 ± 0.002
IR 3 (200)	104.3 ± 0.2	845.5 ± 19.1	0.020 ± 0.002

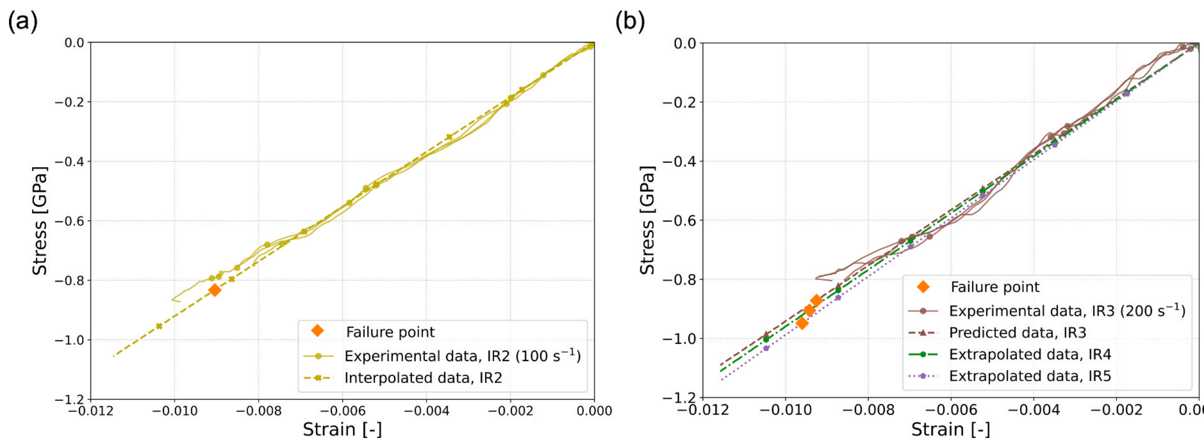

Fig. 5. Predictive capabilities of the CANNs model for the compressive behaviour of IM7/8552 composites: (a) interpolation within the range of training strain-rate, 100 s^{-1} and (b) extrapolation to unseen strain-rates, 300 and 500 s^{-1} (the orange diamond makers indicate the failure).

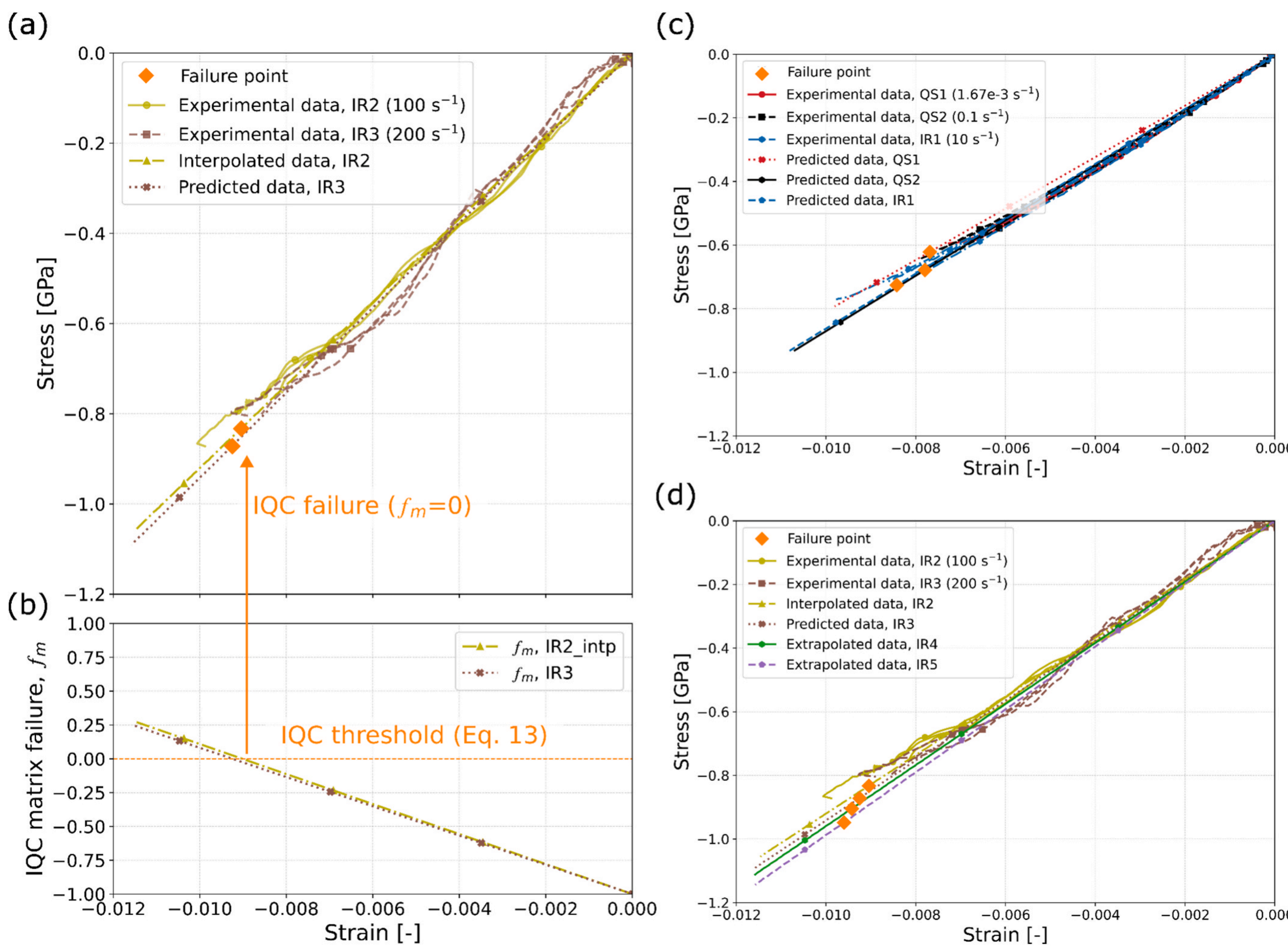

Fig. 6. Assessment of the Constitutive Artificial Neural Networks (CANNs) model performance: (a) experimental versus predicted compressive stress–strain behaviour of IM7/8552 at strain rates of 100 s^{-1} and 200 s^{-1}; (b) determination of failure strength using the Invariant-based Quadratic failure Criterion (IQC); (c) experimental versus predicted compressive stress–strain data of IM7/8552 at strain-rates ranging from 1.67 × 10^{-3} s^{-1} to 10 s^{-1}; (d) experimental versus predicted compressive stress–strain data of IM7/8552 at strain-rates ranging from 100 s^{-1} to 500 s^{-1}.

Table 4
Comparison of experimental and predicted compressive modulus.

Strain Rate [s^{-1}]	Source of data	Experimental modulus [GPa]	CANNs predicted modulus [GPa]	Difference [%]
QS1 (1.67 × 10^{-3})	Experiment	91.1 ± 0.8	79.3 ± 7.1	14.9
QS2 (0.1)	Experiment	89.0 ± 2.1	87.4 ± 0.4	1.8
IR 1 (10)	Experiment	90.2 ± 1.9	87.4 ± 0.9	3.2
IR 2 (100)	Experiment as validation	108.1 ± 5.4	91.7 ± 1.0	17.9
IR 3 (200)	Experiment	104.3 ± 0.2	92.7 ± 2.7	12.5
IR 4 (300)	CANNs prediction	–	93.6 ± 2.9	–
IR 5 (500)	CANNs prediction	–	94.7 ± 3.6	–

Table 5
Comparison of experimental and predicted compressive strength.

Strain Rate [s^{-1}]	Source of data	Experimental strength [MPa]	CANNs predicted strength [MPa]	Difference [%]
QS1 (1.67 × 10^{-3})	Experiment	582.0 ± 26.5	619.9 ± 47.8	−6.1
QS2 (0.1)	Experiment	655.2 ± 26.0	684.9 ± 05.4	−4.3
IR 1 (10)	Experiment	723.4 ± 42.1	722.2 ± 13.1	0.2
IR 2 (100)	Experiment as validation	832.8 ± 48.9	816.1 ± 21.4	2.0
IR 3 (200)	Experiment	845.5 ± 19.1	861.2 ± 31.6	−1.8
IR 4 (300)	CANNs prediction	–	892.2 ± 34.8	–
IR 5 (500)	CANNs prediction	–	938.5 ± 44.8	–

6. Analysis and discussion

6.1. Comparison with analytical model

The Cowper-Symonds (CS) model is a scaling function that based on a semi-logarithmic trend. It has been used to predict strain-rate effect of polymer, and matrix dominated properties [30,32], and is defined as:

$$\sigma = \sigma_{qs}\left(1 + (K\dot{\varepsilon})^{\frac{1}{n}}\right) \tag{21}$$

where, σ_{qs} is the strength at quasi-static condition as reference. $\dot{\varepsilon}$ is strain-rate and two fitting parameters, K and n.

Fig. 7 shows the comparison of normalised compression strength from experiments and predictions from the CANNs model as well as the literature data from [5,6,35–37]. For comparative study, the strain-rate sensitivity of IM7/8552 is empirically estimated using Eq. (21) and the nonlinear least squares method is used to identify three curve fitting parameters. For the literature data, the reported curve fitting parameters ($K = 1.23\text{x}10^{-4}$ and $n = 4.7$) are plotted in dashed purple line while 95% confidence level (± 1.96 × standard deviation) are highlighted in grey colours [32]. In addition, fitting parameters from experimental data in this study is found to be $K = 1.22\text{x}10^{-4}$ and $n = 4.9$. The comparison shows a little difference between the literature data and obtained experimental data (nRMSE = 0.8%). This result indicate that the experimental data obtained from current experimental set-up can be used to generate comparable experimental data.

Furthermore, as discussed in Section 5, the CANNs model demonstrates high flexibility compared to traditional analytical approaches. The CANNs model directly learns the underlying strain energy density function from the data and allows for a more accurate representation of rate sensitivity without manual parameter tuning. Therefore, only a strain-rate value is required to make the prediction once the model is trained. In contrast, phenomenological models such as the CS model are often limited by a pre-defined formulation that may fail to capture complex and competing mechanisms (e.g., matrix cracking and interface failure) present in FRP composites [10]. Thus, the new set of fitting parameters needs to be recalibrated when new data is introduced.

6.2. A limitation of the current CANNs model

6.2.1. A limitation of applying IQC failure criteria

The predicted strength from the CANNs model is lower than experimental and literature data, while the differences are relatively small, experimental data (nRMSE = 7.3%) and literature data (nRMSE = 6.4%). The observed underestimation of the failure strength can be contributed from the formulation of IQC, which explicitly distinguishes between FF and IFF [27,30]. Since the failure threshold ($f_m = 0$) is defined solely by the IFF criterion in this study, it is necessary to confirm whether the observed failure modes from experiments in this study fall within the IFF.

The failure modes of tested specimens are examined via the recorded high-speed images. The high-speed images at the failure varying strain rates are as shown in Fig. 8. The failure mode appears as kink-bands at quasi-static condition and transits to wedge-splitting with increasing strain-rates. Wedge-spitting is associated with two different shear fracture propagating in thickness direction [38] and the IFF criterion is mathematically and physically suited to describe this failure mode. However, the compressive failure of cross-ply laminates is a complex process involving fibre kinking, delamination, and matrix cracking [39]. By limiting the prediction to the IFF mode, the pure fibre compressive failure is effectively excluded from the failure determination. Consequently, the strength predicted from the CANNs model is the onset of matrix instability which acts as a trigger for kinking rather than the later final collapse of the fibres. Therefore, the criterion predicts the onset of the instability and slightly underestimated the final failure load. In the future, fibre compressive failure in kink-band should be considered in the model to increase the prediction accuracy and capture the complex failure mechanism of a cross-ply laminate.

7. Conclusions

This study demonstrates the use of Constitutive Artificial Neural Networks (CANNs) to model the strain-rate dependent, orthotropic behaviour of IM7/8552 carbon/epoxy composites under compression. By directly embedding the constitutive equations for orthotropy and strain-rate dependence into the neural network architecture, the model bridges the gap between continuum mechanics and data-driven ML models.

The results confirm that the integration of physical laws could mitigates the risk of overfitting, which is a common drawback of standard ML approaches. The CANNs model demonstrates data efficiency,

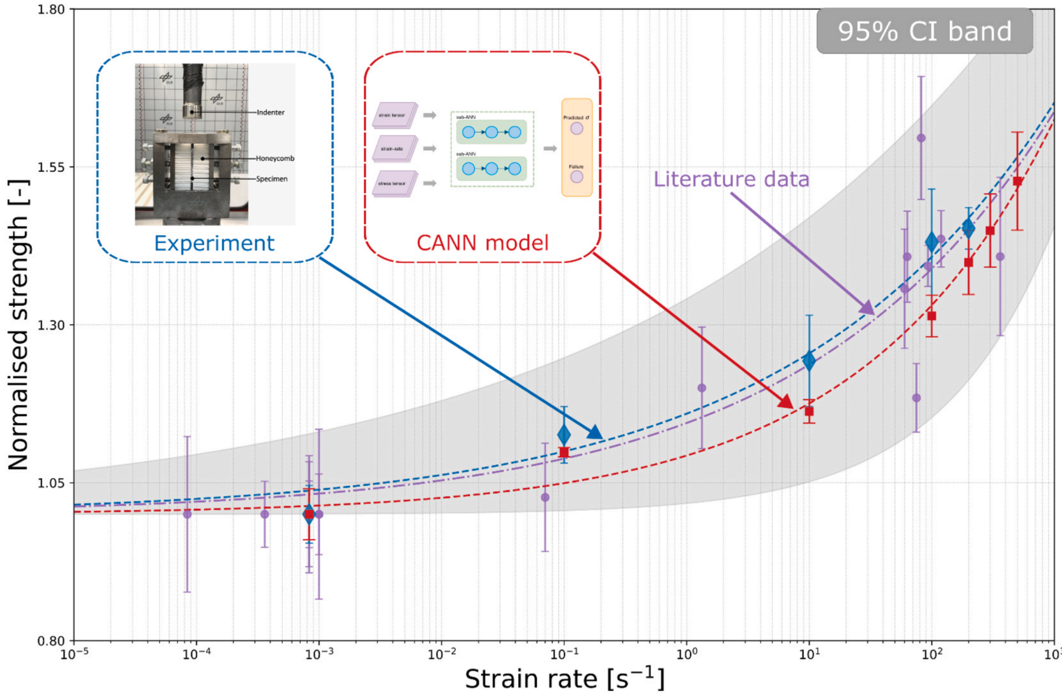

Fig. 7. Comparison of compressive strength of carbon/epoxy composites, both experimental and predicted, in this study with available data in the literature [5,6,35–37].

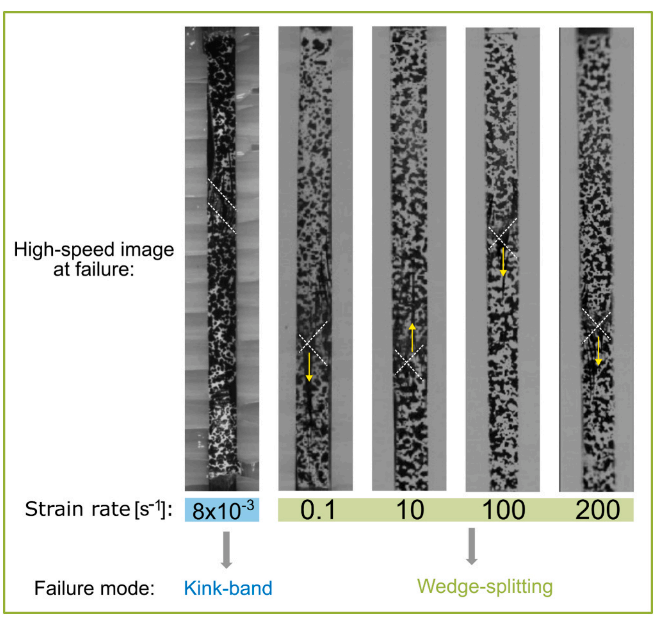

Fig. 8. Failure mechanism at failure occurred during compression testing of cross-ply IM7/8552 composites at different strain rates up to 200 s^{-1}.

effectively learning the constitutive material behaviours with as few as 200 training points per experimental test. Validation against experimental data shows comparatively good agreement, achieving the nRMSE of 7.3%. Also, the implementation of the IQC enables precise identification of failure points, seamlessly linking to matrix failure of FRP composites.

Furthermore, the CANNs model demonstrates robust generalisation capabilities for unseen data. It effectively interpolates rate-sensitive behaviour within the training range while extrapolating to out-of-distribution (OOD) regions. This predictive capacity offers a pathway to accelerate the development of composite structures by significantly reducing the reliance on resource-intensive dynamic testing. Once trained, the model requires only the strain-rate input to generate predictions for unseen loading rates. Finally, the outcome of this work provides a distinct advantage over black-box ML algorithms. The physics-integrated architecture allows that the model behaviour and invariant interactions can be easily interpreted and diagnosed.

Future research should focus on extending this framework to other loading scenarios, such as dynamic shear, and exploring transfer learning techniques. This would allow the full capacity of physics-integrated ML approaches to be exploited, potentially reducing the experimental burdens for new material systems.

CRediT authorship contribution statement

Sanghyun Yoo: Writing – review & editing, Writing – original draft, Visualization, Validation, Methodology, Investigation, Formal analysis, Data curation, Conceptualization. **Ijaz Aslamsha:** Writing – review & editing, Writing – original draft, Visualization, Methodology, Investigation, Formal analysis, Data curation, Conceptualization. **Dipankul Bhattacharya:** Writing – review & editing, Methodology, Investigation. **Julia Kowalski:** Writing – review & editing, Methodology, Investigation. **Nathalie Toso:** Writing – review & editing, Supervision, Resources, Project administration, Funding acquisition. **Heinz Voggenreiter:** Writing – review & editing, Supervision, Funding acquisition.

Declaration of competing interest

The authors declare that they have no known competing financial interests or personal relationships that could have appeared to influence the work reported in this paper.

Appendix A

Material tests are required to determine the nine unknown parameters for orthotropic IQC described in Eq. (13). Based on the proposed stress tensor decomposition in Eqs. (5) and (6), failure surface parameters α_{1-3} can be obtained from shear tests on different planes while the remaining parameters are numerically solved using the rest of equations according to [24,25]. The failure surface equations and corresponding material tests are defined as:

Shear in 1–2 plane

$$\sigma = \begin{bmatrix} 0 & R_{12} & 0 \\ R_{12} & 0 & 0 \\ 0 & 0 & 0 \end{bmatrix}, a_1 = \begin{bmatrix} 1 \\ 0 \\ 0 \end{bmatrix}, a_2 = \begin{bmatrix} 0 \\ 1 \\ 0 \end{bmatrix}$$

$I_1 = 0, I_2 = R_{12}^2, I_3 = R_{12}^2, I_4 = 0, I_5 = 0, I_6 = 0,$

$$f_m = \alpha_2 R_{12}^2 + \alpha_3 R_{12}^2 - 1 = 0$$

Shear in 1–3 plane

$$\sigma = \begin{bmatrix} 0 & 0 & R_{13} \\ 0 & 0 & 0 \\ R_{13} & 0 & 0 \end{bmatrix}, a_1 = \begin{bmatrix} 1 \\ 0 \\ 0 \end{bmatrix}, a_2 = \begin{bmatrix} 0 \\ 1 \\ 0 \end{bmatrix}$$

$I_1 = R_{13}^2, I_2 = R_{13}^2, I_3 = 0, I_4 = 0, I_5 = 0, I_6 = 0,$

$$f_m = \alpha_1 R_{13}^2 + \alpha_2 R_{13}^2 - 1 = 0$$

Shear in 2–3 plane

$$\sigma = \begin{bmatrix} 0 & 0 & 0 \\ 0 & 0 & R_{23} \\ 0 & R_{23} & 0 \end{bmatrix}, a_1 = \begin{bmatrix} 1 \\ 0 \\ 0 \end{bmatrix}, a_2 = \begin{bmatrix} 0 \\ 1 \\ 0 \end{bmatrix}$$

$I_1 = R_{23}^2, I_2 = 0, I_3 = R_{23}^2, I_4 = 0, I_5 = 0, I_6 = 0,$

$$f_m = \alpha_1 R_{23}^2 + \alpha_3 R_{23}^2 - 1 = 0$$

Uniaxial tension

$$\sigma = \begin{bmatrix} R_{1t} & 0 & 0 \\ 0 & 0 & 0 \\ 0 & 0 & 0 \end{bmatrix}, a_1 = \begin{bmatrix} 1 \\ 0 \\ 0 \end{bmatrix}, a_2 = \begin{bmatrix} 0 \\ 1 \\ 0 \end{bmatrix}$$

$I_1 = 0, I_2 = 0, I_3 = 0, I_4 = R_{1t}, I_5 = R_{1t}, I_6 = \frac{-1}{2} R_{1t},$

$$f_m = \alpha_{52} R_{1t}^2 + \frac{1}{4}\alpha_{62} R_{1t}^2 - \frac{1}{2}\alpha_7 R_{1t}^2 + \alpha_{43} R_{1t}^3 + \alpha_8 R_{1t}^3 - \frac{1}{2}\alpha_9 R_{1t}^3 - 1 = 0$$

Uniaxial compression

$$\sigma = \begin{bmatrix} -R_{1c} & 0 & 0 \\ 0 & 0 & 0 \\ 0 & 0 & 0 \end{bmatrix}, a_1 = \begin{bmatrix} 1 \\ 0 \\ 0 \end{bmatrix}, a_2 = \begin{bmatrix} 0 \\ 1 \\ 0 \end{bmatrix}$$

$I_1 = 0, I_2 = 0, I_3 = 0, I_4 = -R_{1c}, I_5 = -R_{1c}, I_6 = \frac{1}{2} R_{1c},$

$$f_m = \alpha_{52} R_{1c}^2 + \frac{1}{4}\alpha_{62} R_{1c}^2 - \frac{1}{2}\alpha_7 R_{1c}^2 - \alpha_{43} R_{1c}^3 - \alpha_8 R_{1c}^3 + \frac{1}{2}\alpha_9 R_{1c}^3 - 1 = 0$$

Biaxial tension

$$\sigma = \begin{bmatrix} 0 & 0 & 0 \\ 0 & R_{2t} & 0 \\ 0 & 0 & 0 \end{bmatrix}, a_1 = \begin{bmatrix} 1 \\ 0 \\ 0 \end{bmatrix}, a_2 = \begin{bmatrix} 0 \\ 1 \\ 0 \end{bmatrix}$$

$I_1 = 0, I_2 = 0, I_3 = 0, I_4 = R_{2t}, I_5 = \frac{-1}{2} R_{2t}, I_6 = R_{2t},$

$$f_m = \frac{1}{4}\alpha_{52} R_{2t}^2 + \alpha_{62} R_{2t}^2 - \frac{1}{2}\alpha_7 R_{2t}^2 + \alpha_{43} R_{2t}^3 - \frac{1}{2}\alpha_8 R_{2t}^3 + \alpha_9 R_{2t}^3 - 1 = 0$$

Biaxial compression

$$\sigma = \begin{bmatrix} 0 & 0 & 0 \\ 0 & -R_{2c} & 0 \\ 0 & 0 & 0 \end{bmatrix}, a_1 = \begin{bmatrix} 1 \\ 0 \\ 0 \end{bmatrix}, a_2 = \begin{bmatrix} 0 \\ 1 \\ 0 \end{bmatrix}$$

$I_1 = 0, I_2 = 0, I_3 = 0, I_4 = -R_{2c}, I_5 = \frac{1}{2} R_{2c}, I_6 = -R_{2c},$

$$f_m = \frac{1}{4}\alpha_{52} R_{2c}^2 + \alpha_{62} R_{2c}^2 - \frac{1}{2}\alpha_7 R_{2c}^2 - \alpha_{43} R_{2c}^3 + \frac{1}{2}\alpha_8 R_{2c}^3 - \alpha_9 R_{2c}^3 - 1 = 0$$

Triaxial tension

$$\sigma = \begin{bmatrix} 0 & 0 & 0 \\ 0 & 0 & 0 \\ 0 & 0 & R_{3t} \end{bmatrix}, a_1 = \begin{bmatrix} 1 \\ 0 \\ 0 \end{bmatrix}, a_2 = \begin{bmatrix} 0 \\ 1 \\ 0 \end{bmatrix}$$

$$I_1 = 0, I_2 = 0, I_3 = 0, I_4 = R_{3t}, I_5 = \tfrac{-1}{2}R_{3t}, I_6 = \tfrac{-1}{2}R_{3t},$$

$$f_m = \frac{1}{4}\alpha_{52}R_{3t}^2 + \frac{1}{4}\alpha_{62}R_{3t}^2 + \frac{1}{4}\alpha_7 R_{3t}^2 + \alpha_{43}R_{3t}^3 - \frac{1}{2}\alpha_8 R_{3t}^3 - \frac{1}{2}\alpha_9 R_{3t}^3 - 1 = 0$$

Triaxial compression

$$\sigma = \begin{bmatrix} 0 & 0 & 0 \\ 0 & 0 & 0 \\ 0 & 0 & -R_{3c} \end{bmatrix}, a_1 = \begin{bmatrix} 1 \\ 0 \\ 0 \end{bmatrix}, a_2 = \begin{bmatrix} 0 \\ 1 \\ 0 \end{bmatrix}$$

$$I_1 = 0, I_2 = 0, I_3 = 0, I_4 = -R_{3c}, I_5 = \tfrac{1}{2}R_{3c}, I_6 = \tfrac{1}{2}R_{3c},$$

$$f_m = \frac{1}{4}\alpha_{52}R_{3c}^2 + \frac{1}{4}\alpha_{62}R_{3c}^2 + \frac{1}{4}\alpha_7 R_{3c}^2 - \alpha_{43}R_{3c}^3 + \frac{1}{2}\alpha_8 R_{3c}^3 + \frac{1}{2}\alpha_9 R_{3c}^3 - 1 = 0$$

Failure surface parameters

$$\alpha_1 := \frac{1}{2}\left(\frac{-1}{\left(R_{12}^0\right)^2} + \frac{1}{\left(R_{13}^0\right)^2} + \frac{1}{\left(R_{23}^0\right)^2}\right)$$

$$\alpha_2 := \frac{1}{2}\left(\frac{+1}{\left(R_{12}^0\right)^2} + \frac{1}{\left(R_{13}^0\right)^2} - \frac{1}{\left(R_{23}^0\right)^2}\right)$$

$$\alpha_3 := \frac{1}{2}\left(\frac{+1}{\left(R_{12}^0\right)^2} - \frac{1}{\left(R_{13}^0\right)^2} + \frac{1}{\left(R_{23}^0\right)^2}\right)$$

Data availability

Data will be made available on request.

References

[1] Brunton SL, Nathan Kutz J, Manohar K, Aravkin AY, Morgansen K, Klemisch J, et al. Data-Driven Aerospace Engineering: Reframing the Industry with Machine Learning. AIAA J 2021;59:2820–47.

[2] Hamm KR, Phillips DR, Imtiaz KS, Raju IS. Revisiting Building Block Approaches for Structures. AIAA SCITECH 2022. Forum 2022:1900.

[3] Liu X, Bai C, Xi X, Zhou S, Zhang X, Li X, et al. Impact response and crashworthy design of composite fuselage structures: An overview. Prog Aerosp Sci 2024;148:101002.

[4] Jin H, Zhang E, Espinosa HD. Recent Advances and Applications of Machine Learning in Experimental Solid Mechanics: A Review. Appl Mech Rev 2023;75.

[5] Koerber H, Camanho pp. High strain rate characterisation of unidirectional carbon–epoxy IM7-8552 in longitudinal compression. Compos A Appl Sci Manuf 2011;42:462–70.

[6] Ploeckl M, Kuhn P, Grosser J, Wolfahrt M, Koerber H. A dynamic test methodology for analyzing the strain-rate effect on the longitudinal compressive behavior of fiber-reinforced composites. Compos Struct 2017;180:429–38.

[7] Perry JI, Walley SM. Measuring the Effect of Strain Rate on Deformation and Damage in Fibre-Reinforced Composites: A Review. Journal of Dynamic Behavior of Materials. 2022;8:178–213.

[8] Yoo S, Vinot M, Deden D, Glück R, Schaefer Y, Toso N, et al. Effect of automated fibre placement (AFP) process induced defects: Dynamic compression properties at intermediate strain rates. J Compos Mater 2025;60:335–51.

[9] Dev B, Rahman MA, Islam MJ, Rahman MZ, Zhu D. Properties prediction of composites based on machine learning models: A focus on statistical index approaches. Mater Today Commun 2024;38:107659.

[10] Dornheim J, Morand L, Nallani HJ, Helm D. Neural Networks for Constitutive Modeling: From Universal Function Approximators to Advanced Models and the Integration of Physics. Arch Comput Meth Eng 2024;31:1097–127.

[11] Furtado C, Pereira LF, Tavares RP, Salgado M, Otero F, Catalanotti G, et al. A methodology to generate design allowables of composite laminates using machine learning. Int J Solids Struct 2021;233:111095.

[12] Ge J, Zhang J, Xu M, Wu M, Yao Z, Fu G, et al. Data-driven CFRP machining performance prediction and optimization: Advances, challenges and future prospects. Thin-Walled Struct 2025;216:113721.

[13] Kibrete F, Trzepieciński T, Gebremedhen HS, Woldemichael DE. Artificial Intelligence in Predicting Mechanical Properties of Composite Materials. Journal of Composites Science. 2023;7:364.

[14] Liu M, Li H, Zhou H, Zhang H, Huang G. Development of machine learning methods for mechanical problems associated with fibre composite materials: A review. Compos Commun 2024;49:101988.

[15] Liu X, Tian S, Tao F, Yu W. A review of artificial neural networks in the constitutive modeling of composite materials. Compos B Eng 2021;224:109152.

[16] Malashin IP, Martysyuk D, Nelyub V, Borodulin A, Gantimurov A, Tynchenko V. Deep learning for property prediction of natural fiber polymer composites. Sci Rep 2025;15:27837.

[17] Shah V, Zadourian S, Yang C, Zhang Z, Gu GX. Data-driven approach for the prediction of mechanical properties of carbon fiber reinforced composites. Mater Adv 2022;3:7319–27.

[18] Sorour SS, Saleh CA, Shazly M. A review on machine learning implementation for predicting and optimizing the mechanical behaviour of laminated fiber-reinforced polymer composites. Heliyon. 2024;10:e33681.

[19] Michaloglou A, Papadimitriou I, Gialampoukidis I, Vrochidis S, Kompatsiaris I. Physics-Informed Neural Networks in Materials Modeling and Design: A Review. Arch Comput Meth Eng 2025.

[20] Raissi M, Perdikaris P, Karniadakis GE. Physics-informed neural networks: A deep learning framework for solving forward and inverse problems involving nonlinear partial differential equations. J Comput Phys 2019;378:686–707.

[21] Wang W, Thai H-T. A physics-informed neural network framework for laminated composite plates under bending. Thin-Walled Struct 2025;210:113014.

[22] Linka K, Hillgärtner M, Abdolazizi KP, Aydin RC, Itskov M, Cyron CJ. Constitutive artificial neural networks: A fast and general approach to predictive data-driven constitutive modeling by deep learning. J Comput Phys 2021;429:110010.

[23] Linka K, Kuhl E. A new family of Constitutive Artificial Neural Networks towards automated model discovery. Comput Methods Appl Mech Eng 2023;403:115731.

[24] Holthusen H, Lamm L, Brepols T, Reese S, Kuhl E. Theory and implementation of inelastic Constitutive Artificial Neural Networks. Comput Methods Appl Mech Eng 2024;428:117063.

[25] Hexcel Corporation 2016.

[26] Kraft H, Holzapfel M. Druckprüfungsvorrichtung für eine Werkstoff-Probe und Druckprüfungsverfahren (DE 10 2016 107 552 B4). Deutsches Patent- und Markenamt: Assignee: German Aerospace Center e.V.; 2016.

[27] Rolfes R, Vogler M, Czichon S, Ernst G. Exploiting the structural reserve of textile composite structures by progressive failure analysis using a new orthotropic failure criterion. Comput Struct 2011;89:1214–23.

[28] Itskov M. Tensor algebra and tensor analysis for engineers: with applications to continuum mechanics. Cham, Switzerland: Springer International Publishing AG; 2007.

[29] Schröder J. Theoretische und algorithmische Konzepte zur phänomenologischen Beschreibung anisotropen Materialverhaltens. Hannover, Germany: Leibniz University Hannover; 1996.

[30] Koerber H, Kuhn P, Ploeckl M, Otero F, Gerbaud P-W, Rolfes R, et al. Experimental characterization and constitutive modeling of the non-linear stress–strain behavior of unidirectional carbon–epoxy under high strain rate loading. Adv Model Simul Eng Sci 2018;5:17.

[31] Vogler M, Rolfes R, Camanho pp. Modeling the inelastic deformation and fracture of polymer composites – Part I: Plasticity model. Mech Mater 2013;59:50–64.

[32] Thomson D, Ploeckl M, Hoffmann J, Lißner M, Pohl C, Quino G, et al. A review of the effect of loading rate on the mechanical properties of unidirectional carbon fibre reinforced polymer composites. Compos A Appl Sci Manuf 2025;193:108773.
[33] Briers WJ. Overcoming Challenges in Material Characterization of Polymers at Intermediate Strain Rates. Cham: Springer International Publishing; 2015. p. 153–64.
[34] Narkhede MV, Bartakke PP, Sutaone MS. A review on weight initialization strategies for neural networks. Artif Intell Rev 2022;55:291–322.
[35] Rouf K, Worswick M, Montesano J. Effect of strain rate on the in-plane orthotropic constitutive response and failure behaviour of a unidirectional non-crimp fabric composite. Compos A Appl Sci Manuf 2024;181:108166.
[36] Thomson D, Quino G, Cui H, Pellegrino A, Erice B, Petrinic N. Strain-rate and off-axis loading effects on the fibre compression strength of CFRP laminates: Experiments and constitutive modelling. Compos Sci Technol 2020;195:108210.
[37] Wiegand J. Constitutive modelling of composite materials under impact loading. UK: Oxford University; 2009.
[38] Opelt CV, Cândido GM, Rezende MC. Compressive failure of fiber reinforced polymer composites – A fractographic study of the compression failure modes. Mater Today Commun 2018;15:218–27.
[39] Sun Q, Zhou G, Guo H, Meng Z, Chen Z, Liu H, et al. Failure mechanisms of cross-ply carbon fiber reinforced polymer laminates under longitudinal compression with experimental and computational analyses. Compos B Eng 2019;167:147–60.